A Multiwavelength Study of Three Solar Flares

M. R. Kundu, A. Nindos[1], S. M. White

Astronomy Department, University of Maryland, College Park, MD 20742

V. V. Grechnev

Institute of Solar–Terrestrial Physics, Lermontov St. 126, Irkutsk 664033, Russia

ABSTRACT

In this paper we seek a self–consistent model for three strong limb flares observed at 17 and 34 GHz by the Nobeyama radioheliograph (NoRH) and also in soft X–rays and hard X–rays by the Yohkoh SXT and HXT instruments. Additional radio spectral data were provided by the Nobeyama polarimeter. The flare geometry is simple with one well–defined flaring loop in each event. The 17 and 34 GHz emission is optically thin gyrosynchrotron radiation from energetic electrons that outlines the flaring loops and peaks close to the loop tops. We infer that the variation of magnetic field along the loops is very small. We try to reproduce the observed radio morphologies and fluxes using a model gyrosynchrotron loop. The results of our modeling rely on the model magnetic field geometry we choose. Although the exact loop geometry cannot be constrained from a two–dimensional snapshot, we choose for simplicity a line–dipole magnetic field and the model field lines are circular. The SXT/HXT images are used to provide the physical parameters of the model loops. The high–frequency polarimeter data give the energy spectral index of the radio–emitting electrons. We could not reconcile the observed radio morphologies and fluxes using classic dipole magnetic field models. The best–fit model that uses the same input parameters for both frequencies and partly reconciles the observed 17 and 34 GHz morphologies and fluxes is produced when we invoke a magnetic field with constant strength along the model loop. These model loops have uniform thickness. The derived densities of the radio–emitting electrons are $1 - 6 \times 10^4$ cm^{-3} with energy limits between 60 and 5000 keV. These models are the best fits we can get under the best assumptions we can justify but they do not in fact match the radio morphologies very well; their problems and limitations are discussed.

Subject headings: Sun: flares – Sun: corona – Sun: radio radiation – Sun: X-rays, gamma rays

---

[1]Present address: Section of Astrogeophysics, Physics Department, University of Ioannina, Ioannina, GR-45110, Greece.

1. Introduction

Electromagnetic emission from solar flares can be detected in practically all wavelengths from gamma rays to kilometer-wavelength radio waves. In order to understand the physical processes involved and obtain a complete picture of a solar flare, multiwavelength coverage with good spectral, spatial and temporal resolution is required. Over the last 20 years several multiwavelength studies of solar flares have been published (eg Alissandrakis, Schadee, & Kundu 1988; Holman, Kundu, & Kane 1989; Wang et al. 1995; Nishio et al. 1997; Hanaoka 1997; Chiuderi–Drago et al. 1998). These studies have helped us to build a unified picture of the flare phenomenon.

Microwave emission from solar flares can provide important diagnostics of acceleration processes in the solar corona because the radio emission is produced by energetic electrons accelerated during the flare. It is well known (e.g. see the reviews by Kundu, & Vlahos 1982; Alissandrakis 1986; Bastian, Benz, & Gary 1998) that the basic emission mechanism of solar microwave bursts is gyrosynchrotron from mildly relativistic electrons (energies of tens to several hundreds of keV) trapped in flaring loops. Gyrosynchrotron emission offers a powerful diagnostic of physical conditions in flaring regions. Unlike X-ray radiation, it is sensitive to magnetic field strength and orientation and can therefore be used to constrain the coronal magnetic field in the flaring source. For a given frequency, the morphology of microwave flare emission depends on the magnetic field configuration (i.e. the geometry of the flaring region and its location on the disk) and the properties of the nonthermal electrons. Usually when the source is optically thick, the maximum intensity occurs close to the loop top. As the source becomes optically thin at high frequencies, emission near the footpoints dominates. However, it will become clear in the following sections of this paper that loop top sources are also possible even in the optically thin case.

The hard X–ray emission of solar flares comes from electrons with energies between 10 and a few hundreds of keV that interact with the ambient protons through the bremsstrahlung mechanism. Using data obtained with the Hard X–ray Telescope (HXT) onboard Yohkoh satellite, Sakao (1994) and Sakao et al. (1994) found that in many cases the HXT imaging data during the impulsive phase of a flare show two components which are observed on each side of the magnetic neutral line suggesting that the two sources are associated with the footpoints of a single flaring loop. The beams of energetic electrons that propagate to the chromosphere heat the chromospheric plasma more rapidly than it can radiate the energy away. Therefore the chromospheric material responds dynamically, expanding mostly along the magnetic field lines. The dense, hot material is expected to move up as a shock hitting the upstream plasma. The upward motion of the heated plasma is known as "chromospheric evaporation". The chromospheric upflow fills the loops with hot, dense plasma (temperatures of $\sim 10^7$ K, densities of $\sim 10^{11}$ cm^{-3}, eg see Aschwanden, & Benz 1997) which emits bright soft X–ray radiation.

In this paper we study three strong flares (GOES classification M3–M6) which were observed with the Nobeyama radioheliograph (NoRH) at 17 GHz and 34 GHz. The flares were also observed in soft X–rays and hard X–rays with the SXT (Soft X–ray Telescope) and HXT (Hard X–ray

Telescope) instruments onboard Yohkoh. We try to reproduce the observed microwave morphologies and fluxes using an inhomogeneous loop model of gyrosynchrotron emission (see Nindos et al. 2000). The Yohkoh data provide important constraints on the input parameters of the models. The SXT images give the shape of the flaring loops and the thermal emission of the flares while the hard X–ray images provide information about the precipitating population of energetic electrons. The HXT data also give the energy spectral index of the electrons that emit hard X–rays with energies between 14 keV and 93 keV. Images of the longitudinal component of the photospheric magnetic field are provided by MDI observations (Michelson Doppler Imager on board SOHO satellite). The gyrosynchrotron models will be compared with the radio observations in an attempt to derive a self–consistent picture of the flare site.

2. Data Analysis

The three flares that we present in this paper were selected after we applied the following criteria to an extended database of Nobeyama observations: (1) Both 17 GHz and 34 GHz NoRH data must be available. (2) The radio emission must show a relatively impulsive rise (i.e. the peak radio emission should be reached within 2–3 min from the onset of the flare). (3) Hard X–ray data from the HXT must be available. (4) Soft X–ray images of the flaring loops must be available, at least for part of the events. The flaring loop configuration that appears in the SXT images must show a simple morphology with one well–defined flaring loop (or arcades of loops) in each event. This criterion immediately rules out both compact loop configurations and complex loop systems.

The Nobeyama radioheliograph (NoRH) consists of 84 antennas in a T–shaped array (Nakajima et al. 1991). It observes the full solar disk in two circular polarizations at 17 GHz and one linear polarization at 34 GHz, with subsecond time resolution for flare events. The data presented here were processed in the NRAO software package AIPS using techniques developed by T. S. Bastian, S. M. White, K. Shibasaki and S. Enome and partially described by Nindos et al. (1999). Since in this study our goal is to achieve optimal spatial resolution, the final images were computed using uniform weighting, cleaned and self–calibrated. The time resolution of the maps that we computed was 15–20 sec. The sizes of the final restoring beams are $10''$–$12''$ at 17 GHz and $6''$–$8''$ at 34 GHz.

All SXT and HXT data were processed with the standard Yohkoh software. When possible, we calculated the electron temperatures and emission measures of the soft X–ray–emitting plasma of the flares using the filter ratio technique (see Hara et al. 1992; Nindos et al. 2000b). The hard X–ray maps were produced using data recorded within 12 sec before and after the maximum hard X–ray peak. The same time intervals were used for the computation of the hard X–ray photon spectral indices γ. For the computation of γ we did not take into account the 14–23 keV channel of the HXT in order to avoid the thermal emission contribution from possible hot sources. Assuming thick target for the production of hard X–rays, the electron energy spectral index is $\delta_x = \gamma + 1.5$ (for the terminology, see e.g. Hudson, Canfield, & Kane 1978; Tandberg–Hanssen, & Emslie 1988; Nitta et al. 1991; Raulin et al. 1999).

Routine MDI observations provide images of the longitudinal component of the photospheric magnetic field. For the 1998 May 8 and the 2000 January 12 events we used MDI images obtained during the flares. For the 1999 August 4 event the MDI image closest to the radio peak was recorded 110 min after the radio peak. The flares that we studied occurred close to the limb, therefore one should treat the information provided by the magnetograms cautiously and try not to overinterpret them.

Our reference time for the co–registrations of the different datasets was the time of the NoRH peaks and the overlays were done using the known pointing information of the instruments. These overlays were checked by comparing the extended preflare thermal emission which is visible in soft X–ray and 17 GHz images. Only in the 2000 January 12 event were the overlays unsatisfactory. In this case, the data co–registration was done by matching the soft X–ray limb with the radio limb (a height of 3000 km was assumed for the soft X–ray limb while the radius of the radio disk was assumed to be 1.0125 times larger than the radius of the optical disk). In all other cases, the agreement was better but in all cases the accuracy of our overlays is not generally better than about $5''$.

3. Observational Results

The three flares that we studied are presented in Figures 1–6. Figs. 1, 3 and 5 show the microwave and hard X–ray images at the time of maximum and also the soft X–ray and magnetogram images which were observed closest to the radio peak. Fig. 2, 4 and 6 show the time profiles of the flare emission at 17 GHz, 34 GHz, hard X–rays (from the HXT) and soft X–rays (from GOES satellite). The NoRH total intensity (I) fluxes are taken from the Nobeyama polarimeter data; the time resolution of the polarimeter data presented here is 1 sec. For the 1998 May 8 event, polarimeter data were not available at 34 GHz and we computed the 34 GHz time profile using the AIPS maps. For all events, the AIPS maps were used for the computation of the circular polarization (V) time profiles. The fluxes from the AIPS maps were computed by summing up all pixels in the flare images with brightness temperatures higher than the lowest contours of Figs. 1, 3 and 5.

The 17 GHz and 34 GHz I time profiles show a good agreement which suggests that the same populations of energetic electrons are responsible for both the 17 GHz and 34 GHz emission. Furthermore the hard X–ray time profiles show the well–known good agreement with the microwave time profiles (e.g. Cornell et al. 1984; Kai, & Nakajima 1987) but a detailed timing study of the radio and/or hard X–ray data is beyond the scope of this paper. The 1998 May 8 radio I time profiles (fig. 2) show an impulsive increase and a much slower decay. We suggest that during the flare the energetic electrons are accelerated more than one time. The 1999 August 4 radio and hard X–ray time profiles (fig. 4) are simpler while the corresponding 2000 January 12 time profiles (fig. 6) reflect the presence of two flares. The radio map movies show that the two flares occurred at the same location (homologous flares). In all three flares the GOES soft X–ray flux peaks well after the microwave/hard X–ray peaks (Neupert 1968).

The Nobeyama polarimeter records total power fluxes at 1, 2, 3.75, 9.4, 17, 34 and 80 GHz. For our three events, the 3.75, 9.4, 17, 34 and 80 GHz fluxes at the time of maximum are given in Table 1. The turnover frequency is between 3.75 GHz and 9.4 GHz for the 1998 May 8 event and the 1999 August 4 event while for the 2000 January 12 event is located between 9.4 and 17 GHz. Therefore the bulk of the radio emission at 17 GHz and 34 GHz is optically thin. Using the fluxes of the radio emissions alone, we cannot determine quantitatively the optical depths at 17 and 34 GHz. However, the radio spectrum in all three events indicates that both 17 and 34 GHz are on the optically thin side of the spectral peak, hence it is appropriate to assume optically thin emission. The 17 GHz emissions will have more opacity than the corresponding 34 GHz emissions, so if there are any optically thick regions they should be at 17 GHz. However, for each event both 17 and 34 GHz maps appear to be identical in morphology, and since the 34 GHz emission must be optically thin, the similarity between the 17 and 34 GHz morphologies reinforces the spectral result that the 17 GHz emission is also optically thin. We used the Nobeyama polarimeter fluxes from 80 GHz to 17 GHz to compute the slope α of the high frequency part of the flare spectrum (for the 2000 January 12 flare we used the 34 and 80 GHz fluxes only). Once α is known, the computation of the electron energy spectral index δ_r is straightforward provided that the emission is optically thin ($\alpha = 1.22 - 0.90\delta_r$, Dulk 1985). We find that $\delta_r = 2.2$, 2 and 2.7 for the 1998 May 8 event, the 1999 August 4 event and the 2000 January 12 event, respectively. These values should be taken as lower limits. The energy spectral index of the hard X–ray–emitting electrons, δ_x is 6.0, 5.8 and 5.0 for the 1998 May 8, the 1999 August 4 and the 2000 January 12 flare, respectively. Discrepancies between the electron energy spectral indices inferred from radio and hard X–ray data during the impulsive burst phase have been reported in several previous studies (eg Kundu et al. 1994; Silva et al. 1997; Raulin et al. 1999). Recently, Silva, Wang & Gary (1999) studied the statistical properties of 28 impulsive flares and found that $\delta_x > \delta_r$ in 74% of them. The large differences between the radio and hard X–ray electron energy spectral indices in the three events that we study raises the question of whether the radio–emitting electrons belong to the same population as the hard X–ray–emitting electrons. The overall similarity between the radio and hard X–ray time profiles is a weak qualitative argument in favor of the common origin of the two electron populations (see, e.g. the review by Gary 2000). Our dataset does not allow us to give a conclusive quantitative answer to the above question (see also the discussion in section 5).

The SXT images in fig. 1, 3 and 5 show the geometry of the flare sites. Both large and smaller loops are present but all three flares occur in the small loops. The 1998 May 8 flare triggered the SXT flare mode and its SXT coverage is excellent. For the 1999 August 4 flare site only full–frame SXT images (FFIs) were available. The only useful image is the one presented in fig. 3. This image was obtained about 6 min before the maximum radio emission which occurred at 05:49:24 UT (there are two more FFIs observed 10 and 9 min before the flare peak but they cannot be used in our study because the flare site is covered by saturated emission). The low–channel HXT map created at the peak of the event shows a loop–like feature which matches the small eastern loop of fig. 3. Therefore no significant changes in terms of the flaring loop geometry are likely to have occurred between the time of the SXT image and the flare peak. The first SXT image of the 2000

January 12 flare was obtained about 9 min after the radio peak which occurred at 01:36:15 UT. However, the shape of the 34 GHz map at the time of maximum delineates fairly well the post–flare loop of fig. 5. Therefore we suggest that that loop represents the flare geometry quite accurately at least to a first approximation.

The flare emissions at 17 GHz and 34 GHz are coincident with the flaring X–ray loops. The 34 GHz sources are smaller than the 17 GHz sources. The true radio flare source sizes can be determined by treating the source in each radio map as the convolution of the true source (assumed to be a two–dimensional gaussian in shape) with the gaussian used for the restoring beam in the map. We can use this technique because the signal–to–noise ratio is adequate. The resulting "deconvolved source sizes" at the time of maximum radio emission for the 1998 May 8 flare are $27'' \times 12''$ at 17 GHz and $25'' \times 10''$ at 34 GHz. The corresponding sizes for the 1999 August 4 flare are $30'' \times 18''$ at 17 GHz and $25'' \times 15''$ at 34 GHz. For the 2000 January 12 flare we get $25'' \times 12''$ at 17 GHz and $17'' \times 8''$ at 34 GHz. The formal uncertainties in the size measurements are in all cases less than $1''$. Therefore the 34 GHz sources appear smaller for two reasons: (1) their true dimensions are smaller than the true dimensions of the 17 GHz sources (2) the restoring beam size decreases with frequency (see section 2). The fact that the true flare source size decreases with frequency has been reported several times in the literature (Gary, & Hurford 1990; Kucera et al. 1994; Kocharov et al. 1994). This well–known effect is due to the inhomogeneity in both the number density of energetic electrons and the magnetic field strength; it does not mean that the lower frequency emission comes from a larger number of electrons. Each flare that we study shows similar time profiles and spatial morphologies at both frequencies; therefore we are confident that the emissions come from the same flaring loop and the same electrons radiate at both frequencies.

The peak of the radio emission is located close to the loop tops. In many cases (eg Shevgaonkar, & Kundu 1985; Nindos et al. 2000) such morphologies have been attributed to optically thick sources: when the emission is optically thick usually the microwave peak occurs at the loop top because the magnetic field is lowest there and therefore the effective energy of the electrons emitting there is higher. Low energy electrons (< 100 keV) can produce optically thick emission at 17 and 34 GHz, but only if the magnetic field is very strong (in excess of 2000 G for emission at 34 GHz) and then the resulting spectrum is inconsistent with the spectra we observe for these events: low energy electrons in such a strong magnetic field produce a peak in the radio spectrum at a very high frequency with essentially no emission above the spectral peak (as in a thermal gyrosynchrotron model, cf. Dulk 1985). We are therefore unable to find a model in which the radio emission at both 17 and 34 GHz can be optically thick and remain consistent with the observed fluxes. All three events occurred close to the limb and the angle between the magnetic field and the line of sight θ can be such that radio emission can be produced from the entire loop even if the emission is optically thin. Of course the only problem in this interpretation is that if the magnetic field is much stronger at the footpoints of the flaring loop then the intensity of the optically thin emission should be higher above the footpoints (eg, see the results from the model computations by Alissandrakis, & Preka–Papadema 1984; Preka–Papadema, & Alissandrakis 1988, 1992; Nindos et al. 2000). The fact that the maxima do not occur above the footpoints implies that the variation of the magnetic field between the footpoints and the loop tops of the three flaring loops is small. Therefore the optically thin radio emission peaks close to the loop tops because the angles θ are larger there. We shall return to these topics in the next sections of the paper.

Both left–hand and right–hand circularly polarized emission appears in the V maps of the three flares. The MDI neutral lines are not reliable because the active regions under study are close to the limb. Therefore no further study of the relationship between the observed V emission and the underlying magnetic field can be made. A comparison of the I and V images in figs. 1, 3, 5 shows that the degree of circular polarization ρ_c is small. The absolute value of typical ρ_c is 10%, 11% and 5% for the 1998 May 8 flare, the 1999 August 4 flare and the 2000 January 12 flare, respectively.

The locations of the three flares close to the limb do not allow an accurate study of the photospheric magnetic field geometry. In order to get more information about the photospheric magnetic field, we also studied the MDI magnetograms obtained on 1998 May 6, 1999 August 2 and 2000 January 14. In all three active regions, the magnetic field changed over 48 hours but comparison of the magnetograms observed closest to the flare peaks with the corresponding magnetograms observed 2 days closer to disk center shows that most of the basic magnetic structures present at the time of the flares are also present 2 days earlier/later. The 1998 May 6 magnetogram shows a pattern consistent with the pattern shown in fig. 1 (the negative polarity, located to the north of the positive polarity, is stronger). The 1999 August 2 magnetogram shows the negative and positive magnetic structures associated with the south footpoint of the August 4 flaring loop. But the negative magnetic patch associated with the August 4 north footpoint of the flaring loop had not developed. In the 2000 January 14 magnetogram, the negative magnetic structure which was associated with the south footpoint of the flaring loop is still present but now a positive polarity patch appears just west of it. On January 12, the magnetic field strength associated with the north footpoint of the flaring loop is much weaker than the field strength associated with the south footpoint of the flaring loop. The same pattern is present in the January 14 magnetogram.

In all three flares the bulk of the emission of the hard X–ray sources in the M1, M2 and H HXT channels is located close to the footpoints of the soft X–ray flaring loops above regions of opposite photospheric magnetic field polarity. Fig. 1 and 5 show that the footpoint hard X–ray sources are asymmetric in the 1998 May 8 flare and the 2000 January 12 flare. In both events the brighter hard X–ray sources are located above the weaker photospheric magnetic field in agreement with the results of Sakao (1994) and Kundu et al. (1995) (the same photospheric magnetic field pattern was present in the 1998 May 6 and 2000 January 14 magnetograms). These properties strongly suggest that the hard X–ray emission in these flares comes from thick–target bremsstrahlung by nonthermal particles.

4. Model Computations

4.1. Input Parameters

The time profiles of the three radio bursts as well as the morphology of the radio images clearly suggest that the 17 and 34 GHz emission is gyrosynchrotron from nonthermal electrons trapped in flaring loops. For the 1998 May 8 event the SXT coverage was excellent and we computed temperatures and emission measures of the soft X–ray–emitting material. The derived plasma parameters were used for the calculation of the 17 and 34 GHz fluxes from the observed soft X–ray–emitting material on the basis of thermal free–free emission (see Dulk 1985, for the formula). The resulting fluxes never exceeded 3 SFU. In this section we present model computations of gyrosynchrotron emission to determine the physical parameters of the three flaring loops. The model has been presented in detail by Nindos et al. (2000). The model uses a line–dipole magnetic field. The field lines are circles with a common tangent point at the dipole: the magnetic field falls off quadratically with distance from the line dipole. The most important physical parameters of this magnetic field model are the magnetic field strengths at the footpoints and at the loop top. The pitch angle distribution of the trapped electrons is assumed isotropic. One may argue that a loss–cone distribution is more appropriate for trapped electrons which produce microwave emission. However, in a loss–cone distribution the electrons missing are those with small pitch angles whose gyro acceleration, and hence emissivity, is smallest. Most of the emission is produced by the larger pitch angles, so using an isotropic distribution should not affect the results significantly. The gyrosynchrotron emission from the loop is computed using a code in which the gyrosynchrotron emissivity and opacity are calculated exactly at specified points along the loop and the emitted radio flux is calculated using simple radiative transfer (Nindos et al. 2000, see also Schmahl, Kundu, & Dennis 1986; Nitta et al. 1991). We shall constrain the input parameters of the models using the observational data that we presented in section 3. The free parameters of the models should be selected so that (1) the models reproduce both the observed morphologies and fluxes of the 17 GHz and 34 GHz emissions and (2) the shape of the model flaring loops is consistent with the shape of the observed flaring loops as inferred from the SXT/HXT images.

The SXT images give the shape of the flaring loops and the hard X–ray sources determine the location of the footpoints of the loops. We choose sets of parameters for the loop geometry (i.e. azimuth, tilt, maximum height and footpoint separation of the model loop) so that the model loops resemble the observed loops. For each event, we kept the coordinates of the model loop equal to the coordinates of the flare site and we varied simultaneously the loop azimuth and tilt angle from -90° to +90° with a step of 10°. Then the best–fit model geometrical input parameters were selected by comparing the projection on the plane of the sky of the resulting model loops with the observed loop using the chi–square criterion (of course some model loops can be ruled out simply by visual inspection). Since the SXT is sensitive to a broad range of temperatures and the SXT images are the convolution of the sky soft X–ray intensity distribution with the SXT's point spread function, the observed thickness of the SXT loops provides upper limits for the thickness of the model loops.

The model loop is filled with energetic electrons with a power–law energy spectral index equal to the power–law energy spectral index of the radio–emitting energetic electrons that we computed in section 3 using the slope of the optically thin part of the Nobeyama polarimeter flux spectra. The photospheric magnetic field strength is ultimately a free parameter in our program because the flares occurred close to the limb and the longitudinal component of the photospheric field that the MDI observes is lower than the total photospheric magnetic field. The other free parameters are the low and high–energy cutoff of the energy distribution of the energetic electrons and also their number density. We did not follow the chi–square criterion for the final selection of the best–fit model because there are too many free parameters for such an approach. For each event, we only seek "qualitatively" good fits, i.e. the same set of input parameters for the model emission at the two frequencies should yield optically thin emission at 17 and 34 GHz with the following characteristics: fluxes roughly equal to the observed fluxes, loop top I maxima (or at least I profiles with no dips close to loop tops) and relatively small degrees of polarization. Varying different free parameters produces changes that we describe here and in Nindos et al. (2000).

4.2. The Best–fit Flare Models

The best–fit model geometrical parameters for the three flaring loops (azimuth, tilt angle, footpoint separation and maximum height of each model loop) are presented in Table 2 (Model I). With these input parameters the projection of each model loop on the plane of the sky is similar to the observed flaring loop as it appears in the SXT images. In our model of circular field lines, loop divergence results in a change of magnetic field strength from the footpoints to the loop top. From the Nobeyama polarimeter data we get the energy spectral index of the trapped electrons (see section 3).

For each event, we tried all possible combinations for the remaining input parameters but we were not able to reproduce both the observed structures and fluxes at 17 and 34 GHz at the same time. In the cases that the model fluxes agree with the observed fluxes, the model morphologies show emission peaks close to the footpoints and a dip close to the loop top. This is not surprising because it is well known (eg Preka–Papadema, & Alissandrakis 1992; Bastian, Benz, & Gary 1998; Nindos et al. 2000) that when the emission is optically thin its maxima are located close to the footpoints provided that the magnetic field is strong at the footpoints and weaker at the loop top. Several previous observations have confirmed this picture (eg Shevgaonkar, & Kundu 1985; Bastian, & Kiplinger 1991; Alissandrakis, Nindos, & Kundu 1993; Wang et al. 1995; Nishio et al. 1997). However, this picture clearly disagrees with the appearance of the flares in the NoRH maps (fig. 1, 3, 5). Another important problem of these models is that the resulting aspect ratios (i.e. loop width/loop length) are implausibly small (of about 0.01 or smaller). On the other hand, the dips at both frequencies disappear if we change the input parameters appropriately and make the model loop optically thick. But the resulting flux spectrum does not agree with the observed flux spectrum (see section 4.3 for details).

The fact that the radio observations show no emission peaks above the footpoints combined with the polarimeter data which indicate that the emission is optically thin at 17 GHz and 34 GHz suggest that the variation of the magnetic field along the loops must be very small. Therefore we tried a model with a constant magnetic field along the loop. In the models presented by Nindos et al. (2000) the loop thickness was scaled along the loop by $B^{-0.5}$ in order to simulate magnetic flux conservation. For a constant magnetic field model, the loop thickness is constant along the loop.

Using the magnetic field model described in section 4.1 but allowing no variations of the magnetic field strength along the model flaring loop, we reached for each flare the best fit to the radio fluxes and structures using a common set of input parameters for both frequencies. These input parameters are presented in Table 2 (Model I). In fig. 7, 8 and 9 we compare one–dimensional profiles of the NoRH maps at the time of maximun flux (top panel) with these model fluxes as a function of distance along the loops, convolved with the appropriate NoRH beam (middle panel). The NoRH profiles were computed along the white curves shown in fig. 1, 3 and 5 (left panels). The white curves were produced by tracing the SXT loops: we selected several points along each flaring loop and we connected them using spline interpolation. In the 1998 May 8 flare the resulting curve is not anchored at the southern HXT source due to overlay uncertainties.

The 17 and 34 GHz model emission is optically thin. Since the model loop is close to the limb, as expected the variation of the angle θ between the magnetic field and the line of sight is not large: $70° < \theta < 87°$. This combined with the fact that the magnetic field is constant along the model loops explains why the variation of the model intensities along the loops is small. Therefore the convolution of the model intensities with the NoRH beam gives flat–top profiles for a significant part of the model loops. The dips close to the loop tops have disappeared. However, the observations show more prominent peak than the models. For each flare, the model polarization shows a dip which is associated with the region where the magnetic field is orthogonal to the line of sight. The degree of circular polarization ρ_c derived from each I and V best–fit model is in rough agreement with the observed ρ_c (within a factor of 1.2–2).

4.3. Optically Thick Models

In all line–dipole field models the loop–top dips at both frequencies disappear if we change the input parameters appropriately and make the model loop optically thick. But the resulting flux spectra do not agree with the observed flux spectra, which indicate that the flux is falling with increasing frequency at 17 and 34 GHz and thus the radio source is optically thin at those frequencies. Using the best–fit model geometrical input parameters, a wide range of the remaining model input parameters can make the 17 GHz model loop optically thick so that its peak is close to the loop top. But in many cases the corresponding 34 GHz models still show a dip close to the loop top. If we make the whole loop optically thick at 34 GHz so that its maximum is close to the loop top then the 34 GHz flux always becomes larger than the corresponding 17 GHz flux (by a factor of 6–7 or more) because the spectrum of optically thick gyrosynchrotron emission is proportional to a high power of frequency. Using our code, the only way to make the fluxes of these optically thick models equal to the observed fluxes is to assume that the transverse dimension of the 34 GHz source is smaller than the transverse dimension of the 17 GHz loop by a factor of about 10 (in our code there is no magnetic field variation in the direction orthogonal to the plane of the loop and the loop's transverse dimension is only used to calculate the resulting flux, which is proportional to it, see Nindos et al. 2000). Such a large difference in the thickness of the two sources can only occur if the magnetic field strength varies dramatically in the direction transverse to the magnetic field lines, implying highly localized currents in the core of the loop. In the bottom panels of fig. 7, 8 and 9 we present the fluxes of these optically thick models as a function of distance along the loop, convolved with the appropriate NoRH beam. The model magnetic field along the loops is also shown. The input parameters that produce these 17 and 34 GHz profiles are presented in Table 2 (Model II). Note that the transverse dimension of the model loops which give the 34 GHz profiles are about a factor of 10 smaller than the transverse dimension of the model loops which give the 17 GHz profiles. Furthermore, the model loop cross–sections are not circular and all transverse loop dimensions are implausibly small, but this is the only way to match the observed fluxes.

5. Discussion

We presented radio, soft X–ray and hard X–ray observations of three strong flares that occurred close to the limb. The geometry of the flares, as inferred from the SXT images, is simple with one well–defined flaring loop in each event. The radio I time profiles in both frequencies show good agreement which suggests that the same population of energetic electrons is responsible for both the 17 and 34 GHz emissions. The 17 and 34 GHz I maps show emission from the entire flaring loops with peaks close to the loop tops. Usually such morphologies are attributted to optically thick gyrosynchrotron emission. However, such an interpretation is not appropriate for our three flares due to the strong support in favor of optically thin emission that the polarimeter data provide. Optically thin radio emission from a limb event can outline the whole loop provided that the flaring loop geometry leads to high angles θ between the magnetic field and the line of sight along the entire loop. The fact that optically thin emission at such high frequencies does not show maxima above the footpoints of the loops may indicate that the variation of magnetic field strength along the flaring loops is very small.

We tried to reproduce the radio spatial structures and fluxes using a simple inhomogeneous gyrosynchrotron model. The SXT and HXT data constrained the geometry of the model loop. The radio spectral data were used for the computation of the energy spectral indices of the model nonthermal electrons. The other input parameters could be varied. Initially, the magnetic field models we used had magnetic field strengths which were higher at the footpoints and weaker at the loop tops. However, such models could not reconcile self–consistently both the observed radio morphologies and fluxes. When the models produced optically thin emission, it was possible to reproduce the observed fluxes but the I models showed maxima above the footpoints and dips close to the loop tops contrary to the observations.

The I model morphology resembles the NoRH maps if we make the loop optically thick at both frequencies. But the resulting radio flux spectra are not consistent with the observations if we use the same input parameters for the model emission at both frequencies. This is because the polarimeter data clearly suggest that the 17 and 34 GHz emissions are optically thin. We note that it is not possible to reproduce self–consistently the observed morphologies at both frequencies by making the model loops optically thick and at the same time keeping the ratios of the model fluxes equal to the ratios of the observed fluxes (even if we do not constrain the absolute values of the model fluxes to match the observed fluxes): if we make the whole loop optically thick at 34 GHz so that its maximum is close to the loop top then the total 34 GHz flux always becomes larger than the corresponding 17 GHz flux (by a factor of 6–7). The only way to make the ratio of the optically thick model fluxes equal to the ratio of the observed fluxes is to assume that the transverse dimension of the 34 GHz source is smaller than the transverse dimension of the 17 GHz source by a factor of about 10. There is no plausible physical reason why the 34 GHz source should be so much narrower than the 17 GHz source: since the same electrons should radiate at both frequencies, these models require a sharp variation in B transverse to its direction on very small spatial scales. Therefore, we rejected them as physically implausible. At the time of maximum radio emission, the width of the true ("deconvolved") 34 GHz source is smaller than the width of the deconvolved 17 GHz source by a factor of 1.2–1.5 (see section 3). If we assume that at each location along the loop the transverse dimension of the radio source is comparable with its apparent width, this result verifies that the optically thick models that we presented in section 4 are physically implausible. Furthermore, the fluxes of such optically thick models can be made equal to the observed fluxes only if both transverse dimensions of the corresponding loops become significantly smaller (transverse dimensions of about 1.5×10^5-1.5×10^7 cm) than the distance between the heights of the upper and lower lines of force which form the loop (which was $3-4\times10^8$ cm). Consequently, these loop cross–sections are not circular and also such transverse dimensions are implausibly small and cannot be supported by the observations. We also note that the resulting degrees of circular polarization ρ_c are significantly lower than the observed ρ_c.

We note that we have not really explored all possibilities of loop geometry because the loop shape is not a free parameter in our code: such a wide parameter space is beyond the scope of this investigation. The results of our modeling rely on the model magnetic field geometry we choose. The exact nature of the magnetic geometry cannot be determined since it can be quite complex. We choose for simplicity a line–dipole magnetic field and the model field lines are circles with a common tangent point at the dipole. Our loop model permits us to investigate the effects of magnetic field variation along the loop, and produces loops which resemble those observed in EUV and soft X–ray observations of flares, but it is certainly possible that more extreme loop geometries may be capable of explaining the observations. We have not investigated asymmetric loops because the observed events have smoothly evolving time profiles and loop morphologies suggesting emission by trapped electrons, which by definition mirror between the same field strength at both ends of the loop and are largely unaffected by any asymmetries present.

The magnetic field strength of a classic model loop is strong at the footpoints and weaker close to the loop top. Such a magnetic field model produces stronger microwave emission close to the footpoints when the emission is optically thin. The ways to suppress/reduce the emission above the footpoints are: (1) if we study a limb event, it is possible that part of the flaring loop is behind the limb. The occultation of the footpoints prevents their strong radio emission from reaching the observer. However in fig. 1 and 5 we have drawn the radio limb on the SXT images and we clearly see that this was not the case for our flares. (2) In the optically thin limit it is very hard to come up with a model in which the loop top appears brightest, because emissivity goes as a high power of B (Dulk 1985) and we were not able to compensate for the lower B at the loop top by a larger line of sight depth at the loop top because the emissivity is proportional to the line of sight depth. That was true of all models that we computed with non–constant magnetic field using different azimuth and tilt angles. One thing that can be done is make the legs of the loop parallel to the line of sight and the loop top orthogonal to the line of sight, but this is rather implausible for events at the limb. Our models rule out such geometrical configuration because the resulting model loops do not resemble the observed loops. (3) Previous observations and modeling have shown flares where the radio source does not reach all the way down to the footpoints of the flaring loop. Such morphologies have been interpreted within the framework of the classic magnetic field loop model using different arguments (see Preka–Papadema, & Alissandrakis 1992; Nindos et al. 2000; Lee, Gary, & Shibasaki 2000). However, fig. 1, 3 and 5 show clearly that in all three flares the radio emission at both frequencies does reach the footpoints but is simply weaker than the emission from the loop tops. The only exception is probably the 34 GHz source of the 2000 January 12 flare which does not reach the northern HXT source. But the gap is small ($< 5''$) and within the uncertainties of the overlays (see section 2).

The final option, namely to keep the magnetic field constant along the loop, produces the models that use the same input parameters for both frequencies and best fit the datasets. The concept of constant magnetic field along the loop suggests that the loop thickness is also constant due to the principle of magnetic flux conservation. In these models the emission is optically thin at both frequencies in agreement with the polarimeter data. With such a magnetic field model we are able to reproduce the observed fluxes and the I model morphologies do not show dips close to the loop tops. These models do not in fact match the radio data very well, but we need to make it clear that they are the best fits we can get under the best assumptions we can justify. The most serious disagreement of these models with the data is that the I radio emission along the loops is flat–topped whereas the observations show more prominent peaks close to the loop tops (the disagreement is more serious in the 1998 May 8 flare and the 2000 January 12 flare). The I models show flat–topped profiles because the magnetic field is constant along the loop and the loops are located close to the limb with such orientation that the angle θ between the magnetic field and the line of sight does not change significantly along the loop. I peaks close to the loop tops can be produced only if we use the non–constant magnetic field model that we tried originally and make the loops optically thick. In the framework of our constant field model such I peaks cannot be reproduced no matter how we vary the remaining free input parameters. We believe that this disagreement may be due to the oversimplified loop geometry that we used. Furthermore, if the magnetic field is constant along a *flaring* loop there is an additional problem that needs to be confronted: how to keep the microwave–emitting electrons trapped in the corona without magnetic mirroring.

Several different parameters of the three best fit models appear in Table 2 (Model I). It is interesting that all models require the presence of high–energy electrons (as high as 5000 keV). If we remove the electrons above about 500 keV, the model fluxes decrease significantly at both frequencies; the high frequency is affected the most (White & Kundu 2000). Our models indicate that the aspect ratios of the flaring loops is about 0.1. Such aspect ratios are in the low end of observed flare loop aspect ratios (see Takahashi 1997, who found that the aspect ratios of flaring loops are usually 0.1–1). We note that the width of the model flaring loops is always lower than the width of the corresponding SXT flaring loops. This may be the result of inadequate SXT spatial resolution. NIXT high–resolution images (Golub et al. 1990) suggest that loop thicknesses may be lower than $1''$, well below the SXT's resolution. An inspection of TRACE movies also shows such thin loops. Another interpetation may be that the energetic electrons in the coronal part of the loop are confined in selected field lines whose total volume is only a fraction of the soft X–ray flaring loop. On the other hand the precipitating electrons can move across field lines more easily in the chromosphere and therefore the process of chromospheric evaporation fills the entire soft X–ray flaring loop with hot thermal plasma.

A comparison between the energy spectral indices inferred from the HXT data and the energy spectral indices inferred from the polarimeter data shows differences of 2.3–3.8 with the hard X–ray indices being larger. Using the thick–target formulas by Hudson, Canfield, & Kane (1978) (see also Raulin et al. 1999) we computed the energy distribution of the hard X–ray–emitting electrons for the time of hard X–ray maximum. We integrated the energy distribution over the range of 20–100 keV and found rough estimates for the number densities of electrons in that energy range. The densities we found are about 100 times higher than the densities of the trapped electrons that produced the radio emission in our models. Since the optically thin gyrosynchrotron flux increases with increasing density and magnetic field, in principle we may reproduce the 17 and 34 GHz fluxes by increasing the model input density and appropriately decreasing the model input magnetic field. But such models show problems because (1) the inferred magnetic field strengths are too low (50–100 G) and such low values cannot be supported easily by the MDI data (2) the frequencies of the spectral peaks decrease and are not consistent with the polarimeter data. The lack of suitable hard X–ray data combined with the fact that the low energy cutoffs in the gyrosynchrotron models are 60–130 keV does not allow us to investigate whether or not these discrepancies between the derived number densities mean that the hard X–ray emission and the radio emission come from different populations of energetic electrons (eg as in the events presented by Kundu et al. 1994).

6. Summary and Conclusions

The study of the three flares can be summarized as follows:

- The 17 and 34 GHz emission is optically thin gyrosynchrotron radiation that peaks close to the loop tops.
- We could not reconcile the observed radio morphologies and fluxes using classic dipole magnetic field models.
- We infer that the variation of magnetic field along the loops is very small: the best–fit self–consistent model that partly reconciles the observed morphologies and fluxes is obtained when we invoke a magnetic field with constant strength along the model loop.
- These models do show problems: the resulting I profiles along the loops are flat–topped instead of being peaked close to the loop top. Such magnetic confurations may also create problems in the trapping of the radio–emitting electrons.

Our study indicates that the current status of solar flare modeling is not completely satisfactory when we seek self–consistent models that reproduce all the observational aspects of a flare in radio, soft X–rays and hard X–rays. Furthermore, our three–dimensional models are static and we do not attempt to follow evolution of flare radio emission. During the HESSI era we will want to follow the 3D evolution from the pre–flare state to the post–flare state. Obviously the complexity of these tasks is great and will require far more sophisticated models.

Acknowledgments

This research at the University of Maryland was carried out with support from NSF grants ATM 96–12738, ATM 99–09809 and INT 98–19917 and NASA grants NAG 5–7370, NAG 5–8192 and NAG 5–7901. We thank the referee for his comments, which led to significant improvement of the paper.

REFERENCES

Alissandrakis, C. E. 1986, Sol. Phys., 104, 207.

Alissandrakis, C. E., & Preka–Papadema, P. 1984, A&A, 139, 507.

Alissandrakis, C. E., Schadee, A., & Kundu, M. R. 1988, A&A, 195, 290.

Alissandrakis, C. E., Nindos, A., & Kundu, M. R. 1993, Sol. Phys., 147, 343.

Aschwanden, M. J., & Benz, A. O. 1997, ApJ, 480, 825.

Bastian, T. S., & Kiplinger, A. 1991, in R. Winglee, A. Kiplinger, (eds) "Max 1991 Workshop No 3", Estes Park, CO., 153.

Bastian, T. S., Benz, A. O., & Gary, D. E. 1998, ARA&A, 36, 131.

Chiuderi–Drago, F., Alissandrakis, C. E., Bentley, R. D., & Philips, A. T. 1998, Sol. Phys., 182, 459.

Cornell, M., Hurford, G., Kiplinger, A. L., & Dennis, B. R. 1984, ApJ, 279, 875.

Dulk, G. A. 1985, ARA&A, 23, 169.

Gary, D. E. 2000, in High Energy Solar Physics –Anticipating HESSI, ed., R. Ramaty & N. Mandzhavidze, p. 297.

Gary, D. E., & Hurford, G. J. 1990, ApJ, 361, 290.

Golub, L., Herant, M., Kalata, K., Lovas, I., Nystrom, G., Pardo, F., Spiller, E., & Wylczynski, J. 1990, Nature, 344, 842.

Hanaoka, Y. 1997, Sol. Phys., 173, 319.

Hara, H. et al. 1992, PASJ, 44, L135.

Holman, G. D., Kundu, M. R., & Kane, S. R. 1989, ApJ, 345, 1050.

Hudson, H. S., Canfield, R. C., Kane, S. R. 1978, Sol. Phys., 60, 137.

Kai, K., & Nakajima, H. 1987, in "Rapid Fluctuations in Solar Flares", NASA Conference Publ., 2449, 147.

Kocharov, L. G., Lee, J. W., Zirin, H., Kovaltsov, G. A., Usoskin, I. G., Pyle, K. R., Shea, M. A., & Smart, D. F. 1994, Sol. Phys., 155, 149.

Kucera, T. A., Dulk, G. A., Gary, D. E., & Bastian, T. S. 1994, ApJ, 433, 875.

Kundu, M. R., & Vlahos, L. 1982, SSRv, 32, 405.

Kundu, M. R., White, S. M., Gopalswamy, N., Lim, J. 1994, ApJS, 90, 599.

Kundu, M. R., Nitta, N., White, S. M., Shibasaki, K., Enome, S., Sakao, T., Kosugi, T., & Sakurai, T. 1995, ApJ, 454, 522.

Lee, J., Gary, D. E., & Shibasaki, K. 2000, ApJ, 531, 1109.

Nakajima H., et al. 1991, Proc. IEEE, 82, 705.

Newpert, W. M. 1968, ApJ, 153, 59.

Nindos, A., Kundu, M. R., White, S. M., Gary, D. E., Shibasaki, K., & Dere, K. 1999, ApJ, 527, 415.

Nindos, A., White, S. M., Kundu, M. R., & Gary, D. E. 2000, ApJ, 533, 1053.

Nindos, A., Kundu, M. R., White, S. M., Shibasaki, K., & Gopalswamy, N. 2000, ApJS, 130, 485.

Nishio, M., Yaji, K., Kosugi, T., Nakajima, H., & Sakurai, T. 1997, ApJ, 489, 976.

Nitta, N., White, S. M., Schmahl, E. J., & Kundu, M. R. 1991, Sol. Phys., 132, 125.

Preka–Papadema, P., & Alissandrakis, C. E. 1988, A&A, 191, 365.

Preka–Papadema, P., & Alissandrakis, C. E. 1992, A&A, 257, 307.

Raulin, J.–P., White, S. M., Kundu, M. R., Silva, A. V. R., & Shibasaki, K. 1999 ApJ, 522, 547.

Sakao, T. 1994 Ph. D. thesis, University of Tokyo.

Sakao, T., Kosugi, T., Masuda, S., Yaji, K., Inda–Koide, M., & Makishima, K. 1994 in Proc. Kofu Symp., A New Look at the Sun, ed. S. Enome & T. Hirayama (Nobeyama: Nobeyama Radio Obs.), 169.

Schmahl, E. J., Kundu, M. R., & Dennis, B. R. 1986, Adv. Space Res., 6, 143.

Shevgaonkar, R. K., & Kundu, M. R. 1985, ApJ, 292, 733.

Silva, A. V. R., Gary, D. E., White, S. M., Lin, R. P., & de Pater, I. 1997, Sol. Phys., 175, 157.

Silva, A. V. R., Wang, H., & Gary, D. E. 1999 in Proc Nobeyama Symposium, ed. T. S. Bastian, N. Gopalswamy & K. Shibasaki.

Takahashi, M. 1997, Ph. D. thesis, Graduate Univ. Adv. Study (NAOJ), Tokyo.

Tandberg–Hanssen, E., & Emslie, A. G. 1988, in The Physics of Solar Flares, Cambridge University Press, Cambridge.

Wang, H., Gary, D. E., Zirin, H., Kosugi, T., Schwartz, R. A., & Linford, G. 1995, ApJ, 444, L115.

White, S. M., & Kundu, M. R. 2000 in High Energy Solar Physics –Anticipating HESSI, ed., R. Ramaty & N. Mandzhavidze, p. 335.

Table 1. Nobeyama Polarimeter Fluxes

Date	Location	GOES Class	Flux 3.75 GHz (SFU)	Flux 9.4 GHz (SFU)	17 GHz Flux (SFU)	34 GHz Flux (SFU)	80 GHz Flux (SFU)
1998-05-08	W82S15	M3.1	42	182	94	65[a]	–
1999-08-04	W64S18	M6.0	246	583	428	208	165
2000-01-12	E79N13	M2.8	300	550	946	582	144

[a]Derived from the flare map.

Table 2. **Model Parameters**

Date	Azimuth [a] (degr)	Tilt [b] (degr)	Footpoint Separation ($\times 10^9$ cm)	Maximum Height [c] ($\times 10^8$ cm)	Thickness [d] ($\times 10^8$ cm)	Transverse Dimension [e] ($\times 10^8$ cm)	B_{foot}[f]/B_{top} (G)	δ_r [g]	Density (cm^{-3})	E_{min}/E_{max} [h] (keV)
1998-05-08 Model I[i]	85	0	3.4	7.5	3.8	3.8	350/350	2.2	1×10^4	60/5000
1998-05-08 Model II[j]	85	0	3.4	7.5	3.8	0.015/0.0015	800/665	2.2	1×10^7	60/5000
1999-08-04 Model I[i]	70	20	2.2	8.8	4.0	4.0	320/320	2.0	4×10^4	70/5000
1999-08-04 Model II[j]	70	20	2.2	8.8	4.0	0.059/0.0048	700/470	2.0	4.5×10^7	70/5000
2000-01-12 Model I[i]	80	0	2.3	13.0	3.2	3.2	370/370	2.7	6×10^4	130/5000
2000-01-12 Model II[j]	80	0	2.3	13.0	3.2	0.15/0.015	870/355	2.7	6×10^7	130/5000

[a] Orientation of the loop with respect to local North.

[b] Angle between the plane of the loop and the local vertical.

[c] Height above the solar surface of the upper line of force which forms the model loop.

[d] Distance between the heights above the solar surface of the upper and lower lines of force which form the model loop.

[e] Transverse dimension of the model loop. Note that in Model II different transverse dimensions have been assumed for the production of the 17 and 34 GHz emissions.

[f] Footpoint and loop top magnetic field strength.

[g] Energy spectral index of the radio–emitting electrons.

[h] Low–energy and high–energy cutoffs of the radio–emitting electrons.

[i] Best–fit self–consistent models. The magnetic field is constant along the loop.

[j] Optically thick models that match the observed morphologies and fluxes; they are not self–consistent.

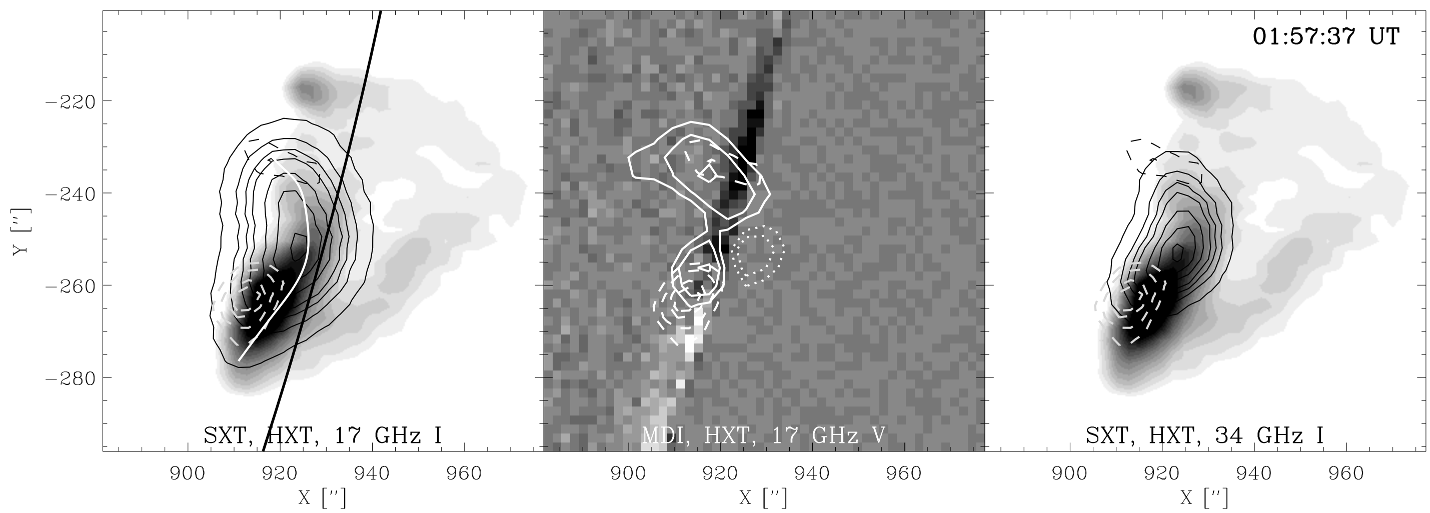

Fig. 1.— The 1998 May 8 flare. The left and right panels show an SXT image obtained 10 sec before the time of the radio maximum. The middle panel shows an MDI photospheric magnetogram obtained 1 min after the flare. The black solid contours show the 17 and 34 GHz I emission at the time of maximum. The contour levels for both frequencies are (5%, 15%, 25%, 35%, 55%, 75%, 95%) of the maximum brightness temperature which is 9.8 MK and 2.4 MK at 17 and 34 GHz, respectively. In the middle panel the white solid and dotted contours show the 17 GHz left–hand and right–hand V emission, respectively. The V contours are at (-10%, $\pm$2.5%, $\pm$5%) of the maximum 17 GHz I brightness temperature. In all three panels the dashed contours show the hard X–ray emission from the M2 HXT channel at the time of maximum. The HXT contours are at (12.5%, 25%, 50%, 70.7%) of the maximum hard X–ray emission. Note that in order to increase the visibility of the HXT contours we have not used the same color for all HXT contours: in the left and right panels we use black and grey for the north and south component respectively; in the middle panel the contours of both HXT components are white. In the left panel, the white curve delineates the flaring loop while the thick black curve shows the radio limb. In this and subsequent solar images, north is up and west to the right. The axes labels denote seconds of arc from disk center. The label in the right top corner of the figure indicates the time of the radio images.

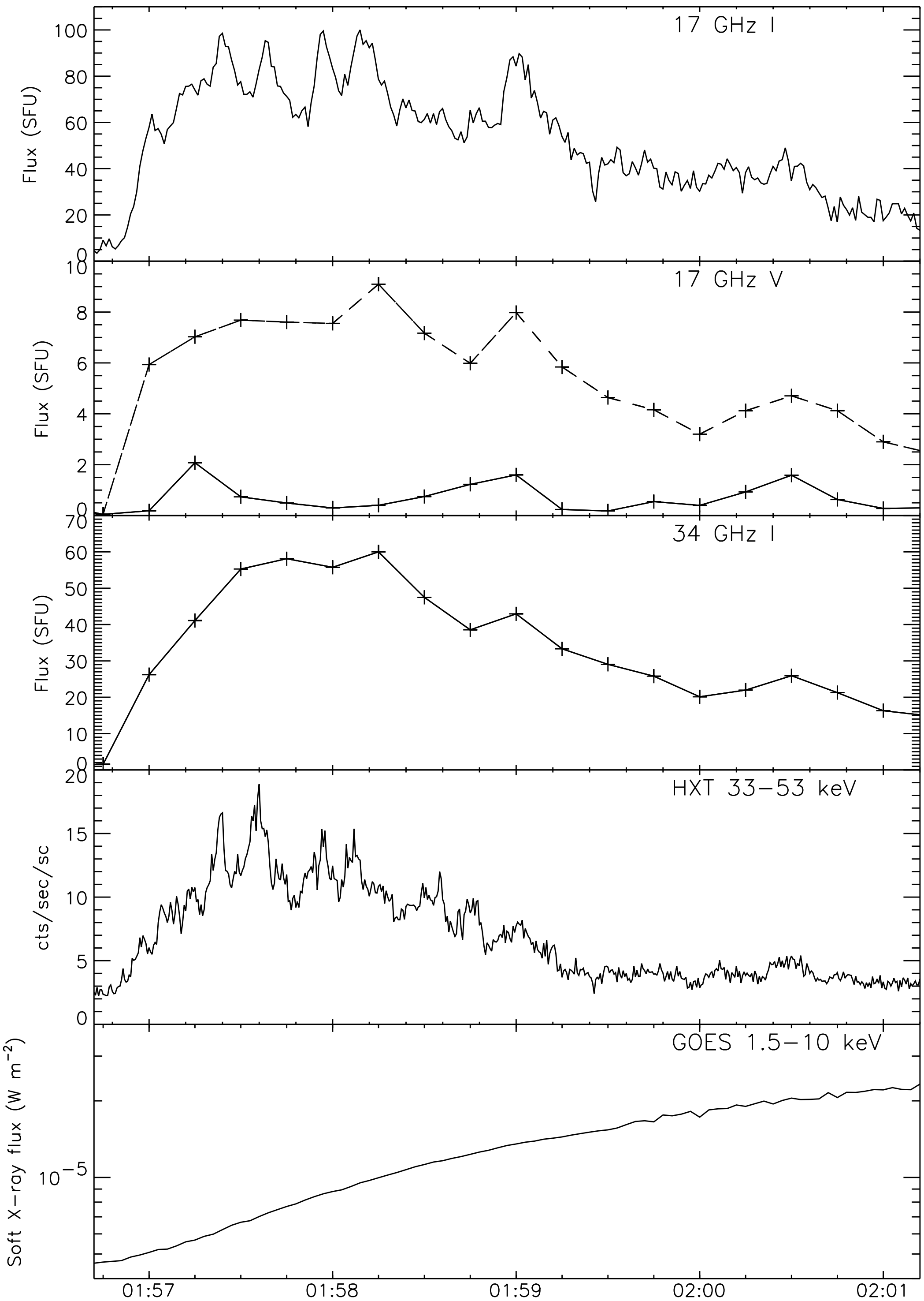

Fig. 2.— Time profiles of the 1998 May 8 flare. From top to bottom: 17 GHz I, 17 GHz V, 34 GHz I, hard X–ray emission in the 33–53 keV HXT channel and soft X–ray emission from GOES 1.5–10 keV data. The 17 GHz I profile has been derived from the Nobeyama polarimeter data at 1 sec time resolution. The 17 GHz V profiles and the 34 GHz I profile have been derived from the AIPS maps at 15 sec time resolution. The dashed and solid V profiles show left–hand and right–hand circularly polarized emission, respectively.

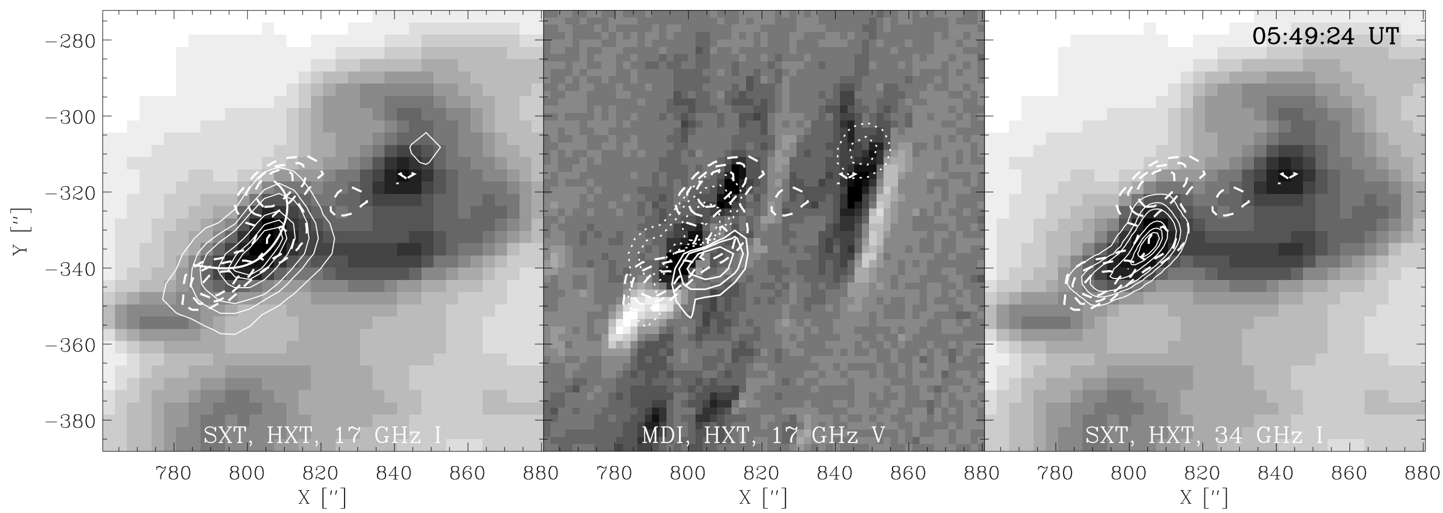

Fig. 3.— The 1999 August 4 flare in the same format as in fig. 1 with the following exceptions. The SXT image was obtained about 6 min before the maximum radio emission. The MDI image was obtained 1 hour and 50 min after the flare peak. In the left and right panels, the white solid contours show the 17 and 34 GHz I emission. The contour levels for both frequencies are (5%, 15%, 25%, 55%, 75%, 85%) of the maximum brightness temperature which is 25.7 MK and 6.9 MK at 17 and 34 GHz, respectively. In the middle panel the dotted and solid white contours show the left–hand and right–hand circularly polarized emission. The V contour levels are at (±2.5%, ±5%, ±10%) of the maximum 17 GHz I brightness temperature. In all panels the hard X–ray emission is denoted by white dashed contours.

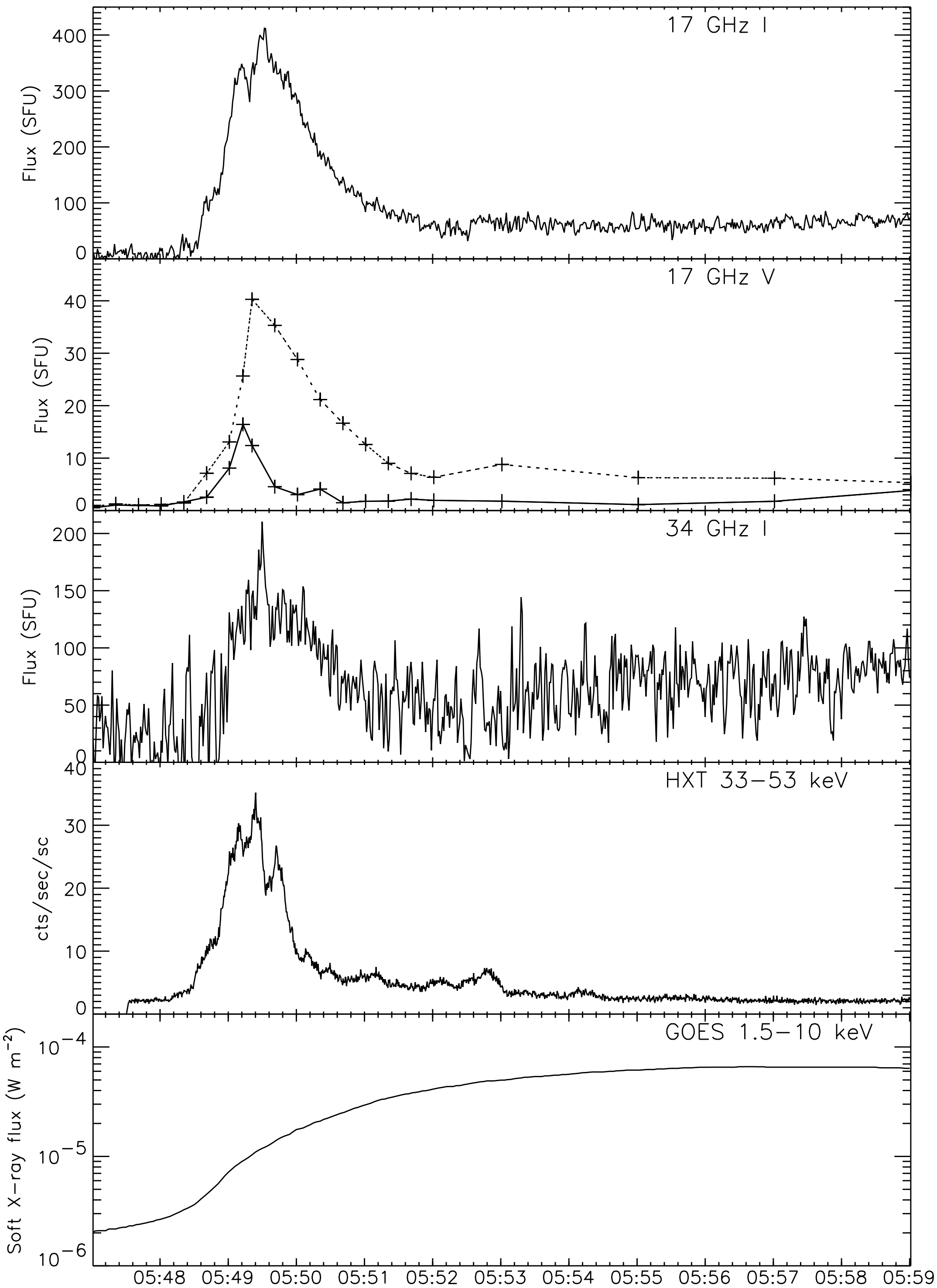

Fig. 4.— Time profiles of the 1999 August 4 flare in the same format as in fig. 2 with the exception that the 34 GHz time profile was derived from the Nobeyama polarimeter data at 1 sec time resolution.

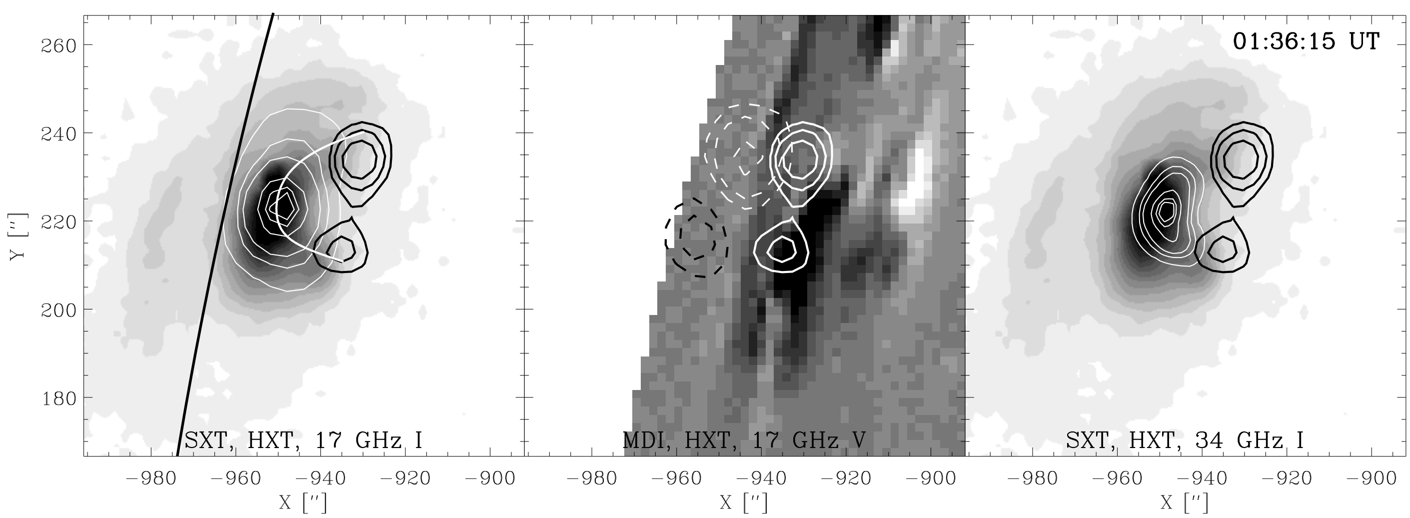

Fig. 5.— The 2000 January 12 flare in the same format as in fig. 3 with the following exceptions. The SXT image was obtained about 10.5 min after the time of the radio maximum and the MDI image was obtained about 6 min after the time of the radio maximum. The maximum brightness temperature is 70.5 MK and 42.5 MK for the 17 and 34 GHz map, respectively. In the middle panel the dashed black and the dashed white contours show the left–hand and right–hand circularly polarized emission. The V contour levels are at (±0.5%, ±1%, 2.5%) of the maximum 17 GHz I brightness temperature. In all panels the thick solid contours show the the hard X–ray emission from the HXT M1 channel. The HXT contours are black in the left and right panel and white in the middle panel.

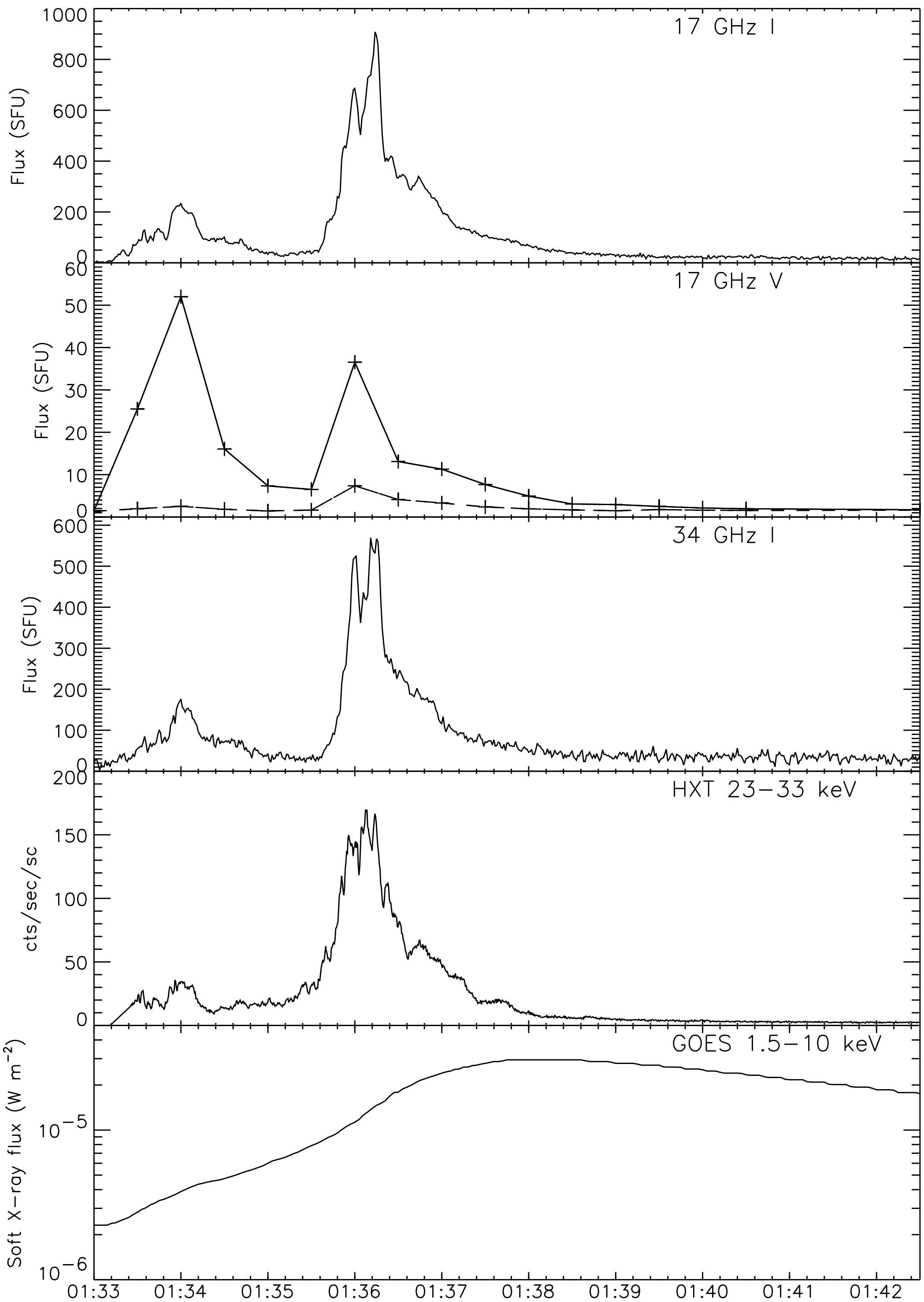

Fig. 6.— Time profiles of the 2000 January 12 flare in the same format as in fig. 4. The only exception is that in this figure the time profile of the hard X–emission from the 23–33 keV HXT channel is presented.

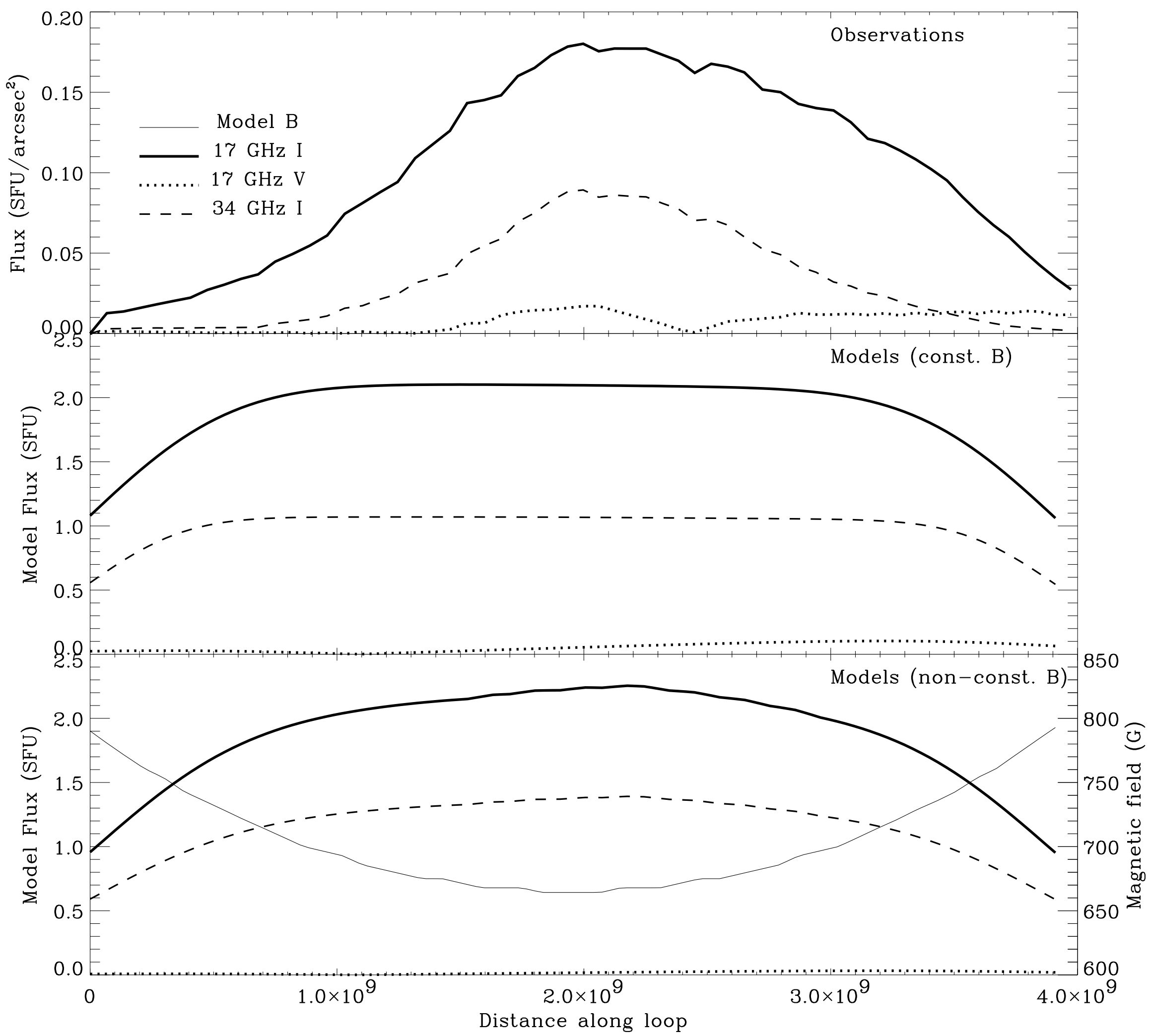

Fig. 7.— Top panel: One-dimensional representation of the 1998 May 8 NoRH flare at the time of maximum. These profiles were computed along the solid white curve shown in the left frame of fig. 1. Middle panel: spatial profiles of the constant–field best–fit models to the 1998 May 8 flare as a function of distance along the loop (see Table 2, Model I for information about the model input parameters). Bottom panel: spatial profiles of the line dipole field best–fit models to the 1998 May 8 flare as a function of the distance along the loop (see Table 2, Model II for information about the model input parameters). In this panel the 17 GHz and 34 GHz model have been computed using different transverse dimensions of the model loop in order to reproduce the observed fluxes. We also present the model magnetic field strength along the loop. For comparison with the observations, each radio profile in the middle and bottom panels has been convolved with the appropriate NoRH beam. In all panels, we present the absolute values of the V profiles. For a better comparison, we have divided the NoRH values with the appropriate beam.

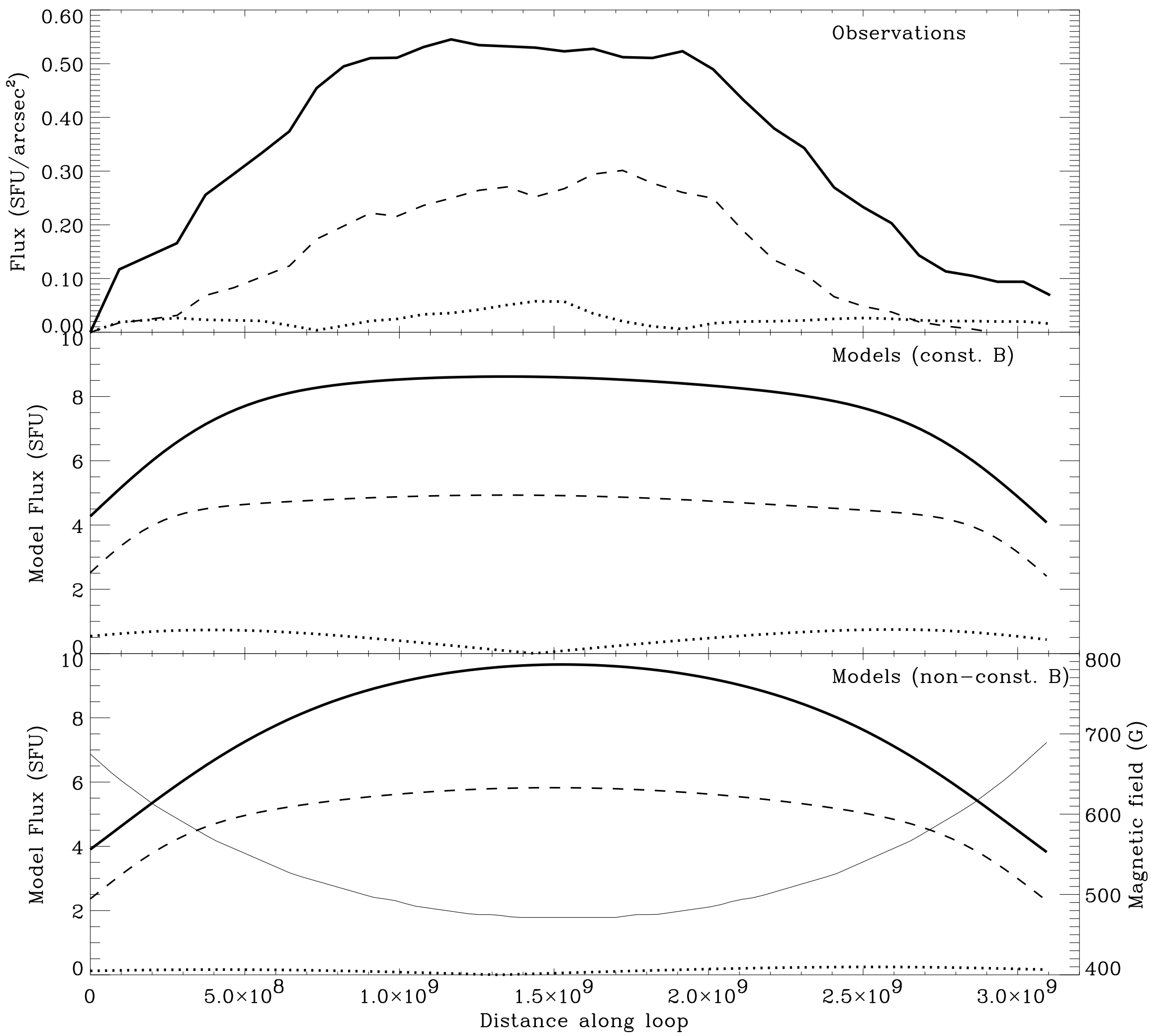

Fig. 8.— Same as in fig. 7 for the 1999 August 4 NoRH maps and models.

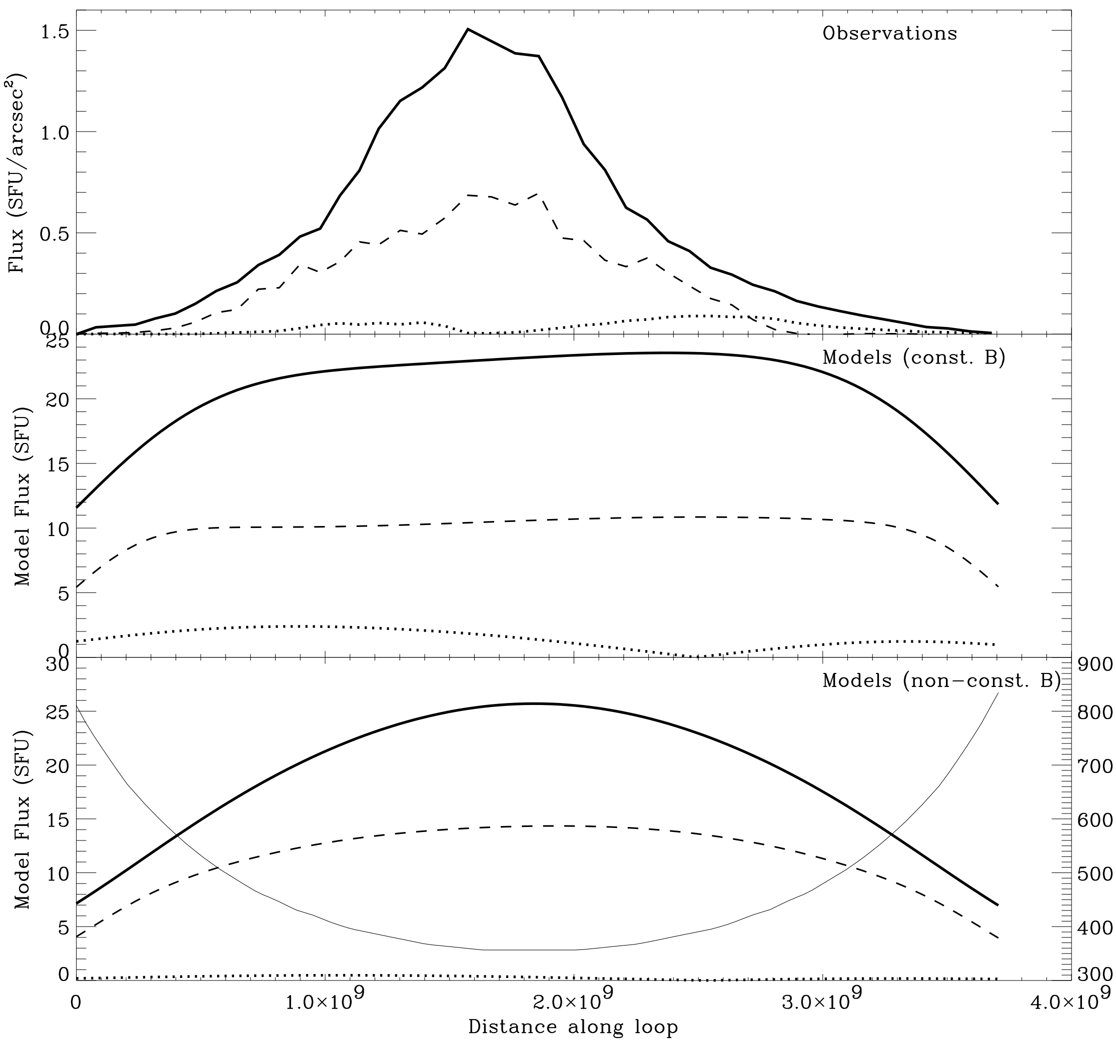

Fig. 9.— Same as in fig. 7 for the 2000 January 12 NoRH maps and models.